A Supervised Multi-Task Learning Architecture for Separating the Phase Contributions in InSAR Burst Modes

Andrea Pulella [*a,b], Pau Prats-Iraola[a], and Francescopaolo Sica[b]
[a]Microwaves and Radar Institute, German Aerospace Center (DLR)
[b]Institute of Space Technology and Space Applications, University of the Bundeswehr Munich

Abstract

Multi-swath SAR systems are attractive solutions for monitoring the large-scale motions occurring over non-stationary areas. The main limitation of such interferometric systems is the variable sensitivity along the flight direction, which results in phase jumps between adjacent bursts in the interferograms. In this paper, we present a convolutional neural network that decouples the interferometric phase from the along-track phase contribution by simultaneously solving multiple tasks, (1) separating the phase due to displacements in the line-of-sight direction from that due to displacements in the along-track direction, and (2) predicting a proxy for the along-track displacement. The benefits of the proposed algorithm are verified using Sentinel-1 TOPS interferometric pairs over Greenland to track the inland glacier flow occurring within a time frame corresponding to the revisit time.

1 Introduction

Burst modes such as Scanning Synthetic Aperture Radar (ScanSAR) [1] and Terrain Observation by Progressive Scans (TOPS) [2] are among the most widely used acquisition modes in SAR satellite missions in order to achieve a large coverage. They offer extensive coverage by cyclically sweeping the antenna beam through different range channels, called subswaths, forming a sequence of SAR image units, named bursts. They are often used in repeat-pass interferometry for topographic mapping in stationary scenarios and for tracking large-scale displacements over non-stationary areas. The main challenge of using the burst mode systems is the retrieval of interferometric outputs along the edges of the bursts. Indeed, the sweep of the antenna beam introduces a dependence on the flight direction, which results in phase discontinuities across the bursts in the mosaicked interferograms whenever motion is present across the overlap area. In the case of stationary scenarios, the phase jumps are minimized by evaluating a global constant azimuth misregistration offset for the whole image. In particular, this global shift is measured as the weighted average of the azimuth offset values estimated in each overlapped area using the Enhanced Spectral Diversity (ESD) [4] approach, which guarantees a significantly higher accuracy than conventional methods such as Spectral Diversity (SD) [3] and Incoherent Cross-Correlation (ICC) techniques [4]. The global misregistration offset approximation does not apply to non-stationary scenarios, because surface displacements are spatially varying within the swath. In the conventional ScanSAR burst mode, this problem can be solved using a 2-look technique [5], which observes the same target on ground two times within a data take and exploits the large spectral separation between at the overlap areas. In the case of the TOPS acquisition mode, we are usually limited by the small overlap area, so the problem has to be approached from a different perspective. TOPS is an advanced multi-swath burst mode in which the antenna beam is further electronically rotated from backward to forward in the flight direction. This property improves and compensates for the image quality in the azimuth direction compared to the conventional ScanSAR mode, guaranteeing a wider burst coverage and reduced overlap areas, which saves data storage. Sentinel-1 (S-1) is the first SAR mission implemented by the European Space Agency (ESA) in the framework of the Copernicus Programme [6]. Its main acquisition mode, the Interferometric Wide swath (IW) mode operated as TOPS mode, provides a large swath width of $250\ km$ at a ground resolution of $5 \times 20\ m$ in range and azimuth, respectively [7]. In this system, the beam swap creates a variable sensitivity to the surface displacement of the interferometric system along the azimuth direction that is difficult to decouple in along-track and across-track (or zero-Doppler) phase contributions.

In this paper, we present a new multi-task convolutional neural network (CNN) to jointly reconstruct the along-track (AT) and zero-Doppler (ZD) phases and a proxy for the associated along-track deformation. Section 2 gives an overview of previously published works to mitigate the TOPS phase discontinuities in non-stationary scenarios. Section 3 describes the proposed methodology and the selected CNN, while Section 4 presents the materials used for the development of this work: the Sentinel-1 acquisitions in the inland region of Greenland and the PROMICE ice velocity maps over the selected site. Section 5 shows (1) a comparison of the network's prediction with the previously described state-of-the-art algorithms on real data and (2) the results on a selected portion of the S-1 IW sub-

*email: andrea.pulella@dlr.de

swath. Section 6 draws the conclusions and outlooks.

2 Related Work

Previous investigations have exploited the spectral separation for a target on ground observed by two consecutive bursts to retrieve an accurate estimation of the along-track displacement. In [8], the authors propose the speckle tracking technique, which consists of a local coregistration to reduce phase discontinuities and increase coherence. First, the authors use the ICC to evaluate the range and azimuth offsets over non-stationary scenarios. After a resampling of the secondary image into the primary grid using the measured offset matrix, a spatially adaptive range and azimuth shift using the SD technique is applied to refine the results. This solution simplifies phase unwrapping because the interferograms no longer have phase jumps, but penalizes the interferometric phase quality since the estimation of the shifts has less accuracy and resolution than the interferometric phase. This approach solves extremely large displacements where the interferometric phase information cannot be used but increases the noise of the interferometric phase over areas with low coherence losing the information of the small displacements. A second methodology published in [9] encourages the usage of the differential interferogram within each overlap area of the swath to initialize an image inpainting algorithm, which fills in the gaps between the overlaps using auxiliary offsets estimated from the external DEM. As a result, it returns the zero-Doppler interferometric phase. Although reliable information is present in the overlap areas, the usage of inpainting requires (1) the implementation of a 2-D phase unwrapping, which might be subject to errors in complex scenarios, and (2) a considerable computational time. In addition, (3) the prediction obtained using the inpainting algorithm might be visually meaningless, especially in the gaps.

3 Methodology

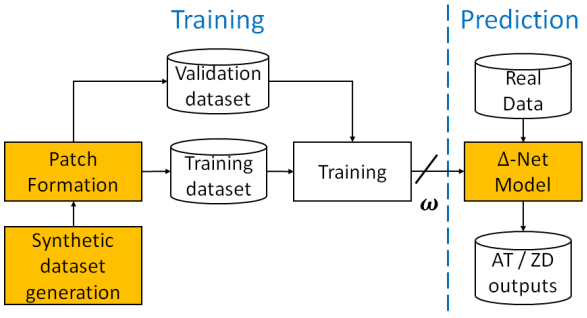

Figure 1 Workflow of the Δ-Net. Blocks in orange highlight the innovative aspects of the presented work.

In this paper, we frame the problem of phase discontinuities across the TOPS bursts in non-stationary scenarios as a phase source separation problem, proposing a CNN architecture and a multi-task supervised learning strategy specifically designed for TOPS interferometric data.
Fig. 1 shows a general overview of the supervised convolutional neural network for the interferometric phase source separation problem. During the training phase, the CNN learns by iteratively adjusting the weights (ω) to predict the correct output for a given set of synthetic inputs. The resulting model is used for the prediction. In the paper, we are indicating the proposed neural network as Δ-Net, where the acronym "DELTA" stands for *DEformations over Land using TOPS burst Alignment*. In the following, we describe in three separate sections the blocks depicted in orange in Fig. 1.

3.1 Synthetic dataset generation

We generate the synthetic interferometric pair of acquisitions by applying a reverse approach. Given a user-defined desired coherence and the noise-free interferometric phase after the event, the signal model induces the displacement in the secondary acquisition (i.e. after the event) and, therefore guarantees data dedicated for the specific motion. The displacement maps are selected by different sources: external surface deformation maps, such as the ice velocity maps produced as part of the Programme for Monitoring of the Greenland Ice Sheet (PROMICE) [10], and more sophisticated mathematical models, such as the one proposed by Okada for the description of seismic events [11]. As a result, a set of synthetic TOPS interferograms are provided to the patch formation step, responsible for the training and validation set splitting.

3.2 Patch formation

We suggest a methodology for patch extraction based on the geometric properties of TOPS systems, such as the position of the junction between two merged TOPS bursts and the size of each burst. In particular, the patch size is tailored to guarantee a centering in the phase jump and, at the same time, to ensure the final aggregation of the predicted patches. The generation of the patches is system-based, in the sense that their dimension and their selection depend on geometric properties of the TOPS data. In particular, this choice results in the selection of a specific window, Ω, when applying multilooking to the interferogram.

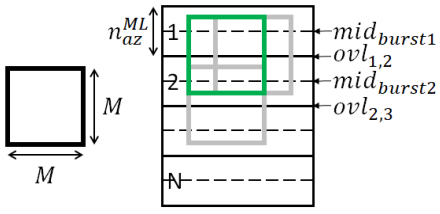

Figure 2 Applied strategy for extracting patches within a TOPS sub-swath. The squares represent the patches located at mid-overlap and the multi-looking (ML) window size is chosen to guarantee a minimal overlap among the consecutive $M \times M$ patches along the azimuth direction.

For instance, in the case of Sentinel-1, since the window

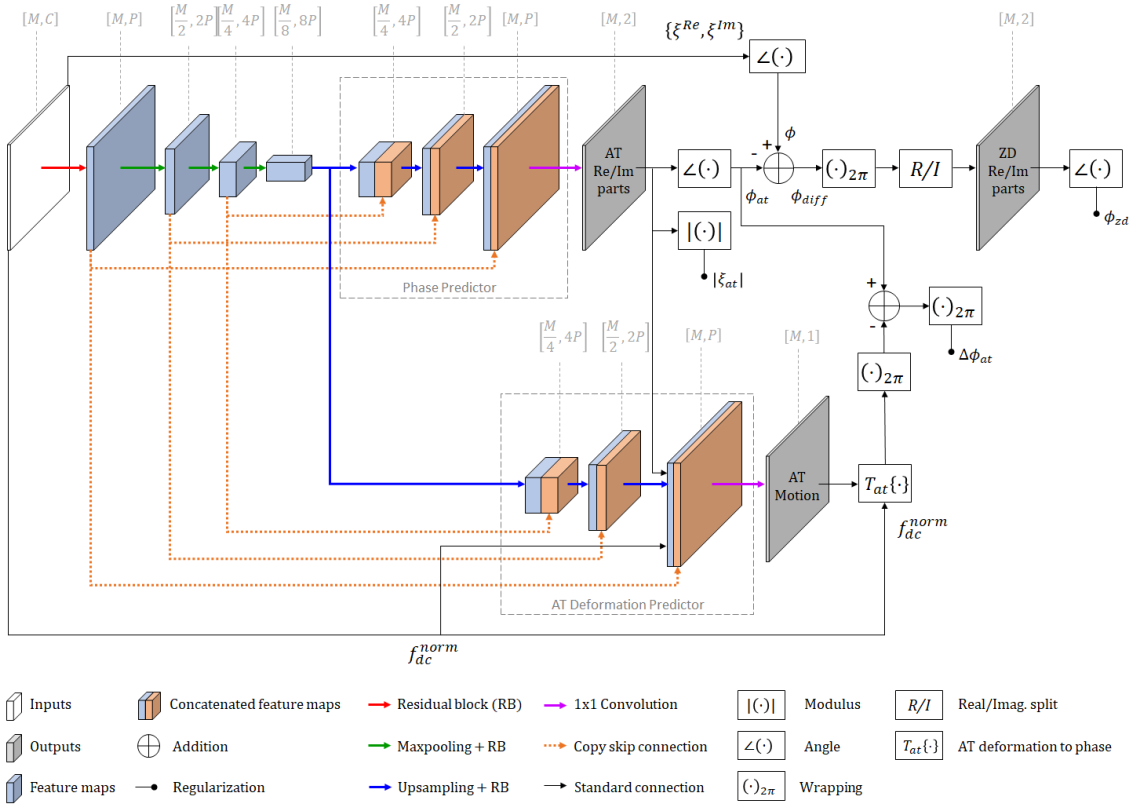

Figure 3 Proposed network architecture. The output dimensions at every single layer are shown in gray brackets. For the sake of simplicity, the used notation implies that the first dimension (i.e., M) identifies a 2-D ($M \times M$) array.

size is chosen according to the azimuth and ground range resolution of IW mode data, we set the output sampling to 100 m, which corresponds to a 7×27 averaging window size. Fig. 2 shows the main advantage of using this assumption. From the subswath point of view, this approach guarantees the splitting in patches located at mid-overlap (green). Indeed, since the burst duration in an S-1 IW product is around 3 s and the azimuth time spacing is approximately equal 2 ms [7], the nominal burst size along azimuth is always around 1500 lines at full resolution. After debursting and multilooking the effective burst size along azimuth, i.e. n_{az}^{ML} in Fig. 2, is around 214 pixels, which is suitable for a $M = 256$ patch size and for guaranteeing an overlap between the patches.

3.3 Δ-Net model

The peculiarity of our proposed strategy is the way we train the network using a multi-task learning strategy, i.e., we simultaneously estimate the two phases to be separated (in along-track and in across-track) and the displacement in the along-track direction. Fig. 3 shows the scheme of the general functioning of our proposed approach.

First, the Δ-Net considers $C = 4$ input variables represented in Fig. 4: the (a) real $\xi^{Re} = Re\{\xi\}$ and (b) imaginary $\xi^{Im} = Im\{\xi\}$ parts of the interferometric phase, (c) the associated coherence ρ, and (d) a map describing the sensitivity of the TOPS primary image retrieved by adding a linear azimuth dependency to each S-1 Doppler centroid range variant vector f_{dc}^{norm}.

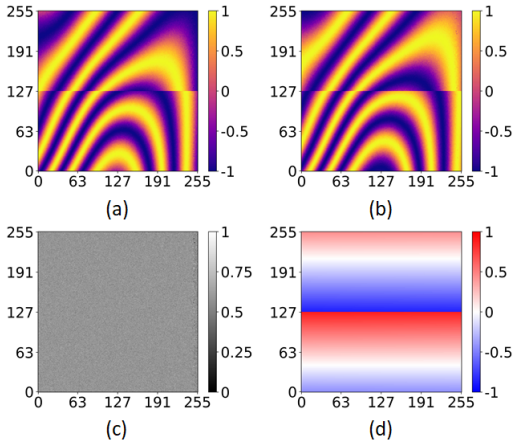

Figure 4 Input features used on a patch located at mid-overlap: (a) and (b) are the real and imaginary parts of the interferometric phasor, denoted in the paper as $Re\{\xi\}$ and $Im\{\xi\}$, respectively; (c) is the interferometric coherence ρ, while (d) is the normalized Doppler centroid f_{dc}^{norm}.

Therefore, in Fig. 3 we can observe that the Δ-Net is based on the U-Net model [12]. In particular, one layer is removed from the original implementation, using a three-layer design for the encoder-like and decoder-like blocks. The former is followed by a bridge layer and two branches, each one comprising a three-layer predictor with skip connections: the upper branch estimates the real and imaginary

parts of the along-track phasor $(\xi_{at}^{Re}, \xi_{at}^{Im})$, then uses the reconstructed along-track phase ϕ_{at} together with the interferometric phase ϕ associated with the real and imaginary parts (ξ^{Re}, ξ^{Im}), i.e., the inputs of the network, for predicting the zero-Doppler phase, ϕ_{zd}, directly derived from the corresponding real and imaginary parts $(\xi_{zd}^{Re}, \xi_{zd}^{Im})$. The same reconstructed along-track phase is used in comparison with the same phase measured from the output of the lower branch, i.e., the along-track displacement u_{at}. In particular, given the normalized Doppler centroid frequency f_{dc}^{norm} used as input to the network, it is possible to apply a root mean square error (RMSE) regularization on the along-track phase estimated in the upper branch and on the same quantity estimated starting from the along-track displacement in the lower branch. In this way, the network is able to set the weights on both branches in order to satisfy even the relationship among the outputs. In addition, regularizations on the unitary modulus in the along-track phasor ξ_{at} and on the continuity of the zero-Doppler phase ϕ_{zd} are considered during the training.

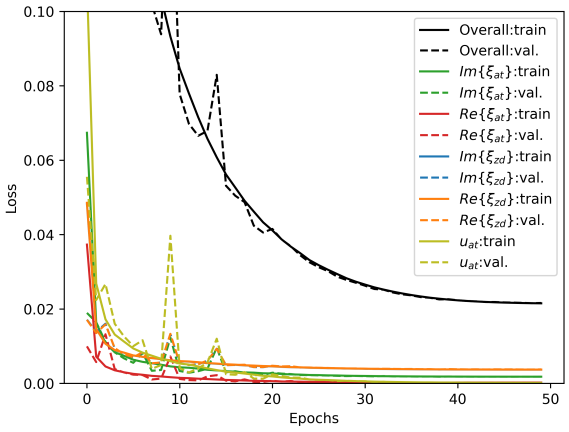

Figure 5 Loss function convergence graph for training (solid) and validation (dashed) using overall 50 epochs. Real and imaginary components of the zero-Doppler phasor, ξ_{zd}, are depicted in orange and blue, respectively, and are overlapped. Real and imaginary parts of the along-track phasor, ξ_{at}, are marked in red and green, respectively. Along-track displacement, u_{at}, is drawn in olive, while the overall loss function is highlighted in black.

Fig. 5 shows that the loss curves are scaled to the same value because we selected the RMSE loss function in all the tasks. The orange and blue curves are respectively associated with real and imaginary components of the zero-Doppler phase and are overlapped. This result is in agreement with the absence of phase jumps in the zero-Doppler phase. On the contrary, the loss functions of the real and imaginary components of the along-track phase drawn respectively in red and green are different because the imaginary part of the along-track phase contains the main information about the phase jump.

4 Materials

Training and test stages have been conducted over Greenland by geographically separating a set of Sentinel-1 acquisitions in the inland region.

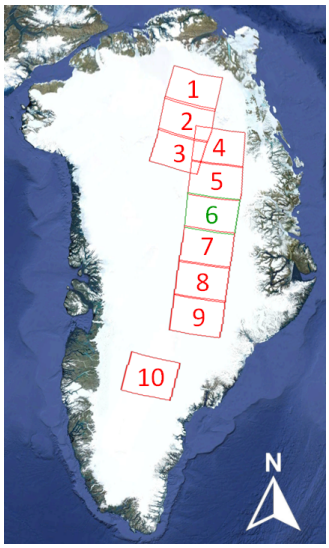

Figure 6 Overview of the S-1 footprints selected as training and test data set over Greenland, superimposed to an optical image from Google Earth. Footprint number 6, indicated as a green rectangle, is used for testing the pretrained network.

The training data set has been created following the patch formation strategy described in Section 3.2 and considering the nine red footprints drawn in Fig. 6. Several synthetic interferometric pairs have been generated by inducing on the secondary SAR image the displacement associated with the ice velocity maps of the PROMICE project. This external data set consists of mosaicked products describing the displacements, in meters per day, occurring in the whole Greenland during the Winter season. In our work, we selected the six available products from Winter 2016-2017 to Winter 2021-2022. Each geospatial product spans between November 1 and February 28 the following year, with a nominal grid spacing of 500 m, including all the ascending and descending SAR images acquired in this time frame.

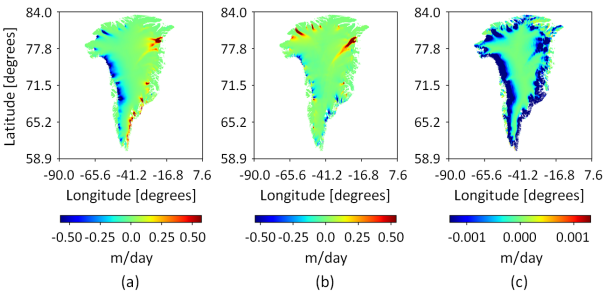

Figure 7 From left to right: (a) East, (b) North, and (c) Vertical components of the ice velocity map retrieved on Winter 2021-2022 [13].

For example, Fig. 7 shows the ice velocity map measured in Winter 2021-2022 over Greenland and displayed as ENU components, projected in the World Geodetic System (WGS84). The remaining green footprint in Fig. 6 has been only used to test the network, as we selected a 12-day real interferometric pair with a negligible ionospheric contribution.

5 Experimental Results

In the following, we present the results using a real interferometric pair acquired in a time frame of 12 days during the Winter season over an inland region in Greenland.

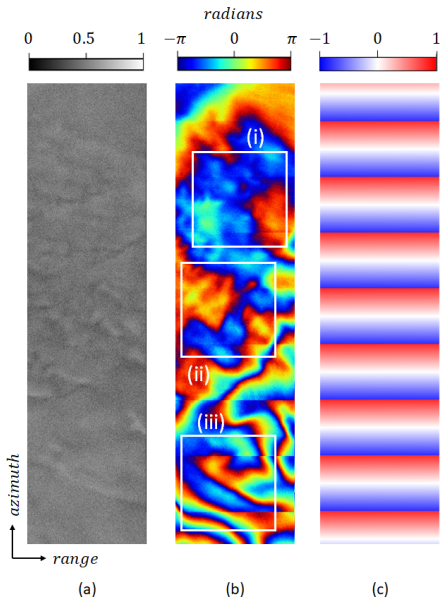

Figure 8 Input features extracted from a real interferometric pair over Greenland. From left to right: (a) coherence ρ, (b) interferometric phase ϕ, and Normalized Doppler-centroid frequency f_{dc}^{norm}. Three sample patches *(i)*, *(ii)*, and *(iii)* of 256×256 pixels are marked with white squares.

For the sake of simplicity, we selected a vertical strip from one of the three S-1 IW subswaths associated with the interferometric pair, and in Fig. 8 we report the input quantities: (a) the coherence ρ, (b) the associated interferometric phase ϕ, and (c) the sensitivity map f_{dc}^{norm}. As expected, the coherence appears almost uniform and on average close to 0.7. On the contrary, in Fig. 8(b) we can notice the phase discontinuities in the azimuth direction; in particular the phase jumps at the beginning of the strip look larger than the ones at the end of it, hence indicating a larger along-track displacement. Furthermore, we can notice that the interferometric phase jumps are linked with the comb-like profile of the sensitivity map in Fig. 8(c), obtained by normalizing the Doppler centroid matrix for $2.8\,KHz$, a value not exceeded in S-1 TOPS data [7], that guarantees the feature to be between -1 and 1.

In order to better analyze our result with the previous methods, we selected three sample patches of 256 × 256 pixels from Fig. 8(b) highlighted with white squares and denoted as *(i)*, *(ii)*, *(iii)*. Fig. 9 compares the results of three different methodologies. First, we can see that in all the patches the correction of the phase jumps in the input data, presented in column (a), is better performed using the Δ-Net, whose results are shown in (d).

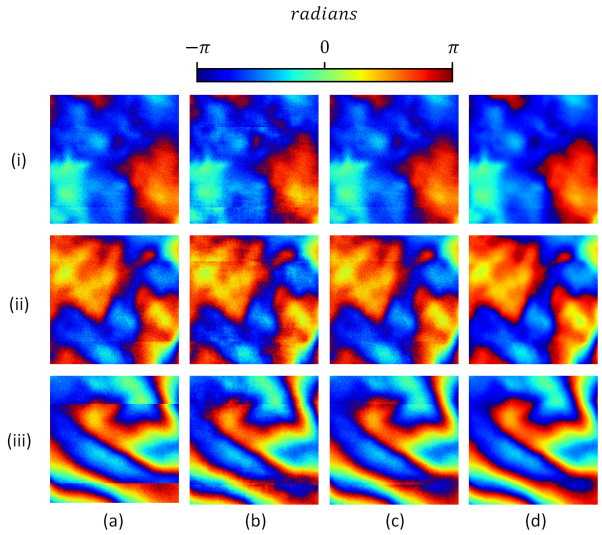

Figure 9 Predictions using different methodologies (columns) on different patches (rows). From left to right: (a) interferometric phase used as input to the network, and zero-Doppler phase reconstructed using (b) speckle-tracking [8], (c) image inpainting [9], and the proposed (d) Δ-Net. Both the three sample patches *(i)*, *(ii)*, and *(iii)* are selected with white 256×256 squares in Fig. 8.

Both speckle tracking and image inpainting do not fully mitigate the discontinuity. The former, reported in column (b), introduces noisy jumps over the patches *(i)* and on the top overlap of patch *(ii)*. The latter, reported in column (c), appears in general more robust thanks to the DEM-based image inpainting applied to the deformation linked with the differential interferogram. On the other hand, we might associate the slight residual jumps in patch *(iii)* of column (c) to the implementation of the inpainting methodology which is overwriting part of the known information stored in the overlapped areas.

Fig. 10 shows the final aggregation of the patches predicted from the input features reported in Fig. 8. The phase jumps are almost completely removed in the zero-Doppler phase ϕ_{zd} in Fig. 10(a). By comparing the predicted along-track parameters, ϕ_{at} in Fig. 10(b) and u_{at} in Fig. 10(c), we can see a matching with the jumps in the interferometric phase ϕ, in Fig. 8(b). In particular, the higher the density of fringes in the overlap area of ϕ, the greater the discontinuity in ϕ_{at}, which corresponds to a large deformation in the along-track direction u_{at}. Furthermore, we can observe that the along-track motion is accurate on the overlap but is an approximation at mid-burst because of the different sensitivity along the TOPS burst.

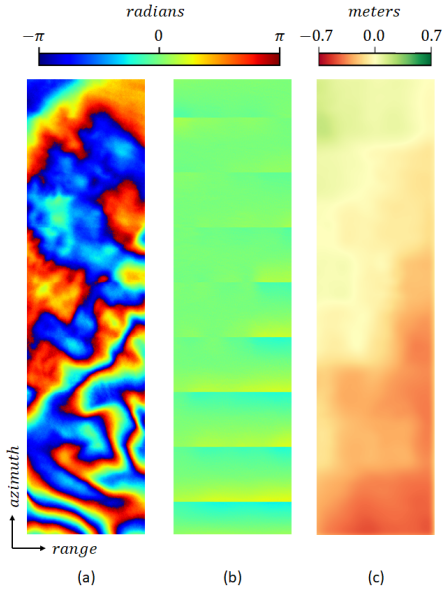

Figure 10 Output features predicted by the Δ-Net. From left to right: (a) zero-Doppler phase ϕ_{zd}, (b) along-track phase ϕ_{at}, and along-track displacement u_{at}.

6 Conclusions and Outlooks

The current work presents a supervised multi-task learning architecture for separating the phase contributions due to zero-Doppler and along-track displacements. The approach of fusing SAR system models with machine learning techniques demonstrates physics-based machine learning in our network architecture and loss functions. Results over an inland glacier flow in Greenland using Sentinel-1 interferometric wide-swath data show the outstanding performance of the proposed network in estimating displacements ranging from a few centimeters to tens of centimeters. In addition, our method solves the limitations of speckle tracking to properly estimate small displacements and offers greater robustness in handling diverse deformation patterns compared to burst-overlap differential phase-based methods. The technique could be exploited for monitoring glaciers in the Arctic, e.g., over Greenland by using Sentinel-1 data, measuring large deformations over ice land areas, e.g., glacial flows, but also over solid earth, e.g., earthquakes. Finally, we believe that the proposed approach could mitigate the phase jumps present in TOPS interferograms in the presence of along-track motion in the scene as a generalization of the ESD technique.

7 Literature

[1] Holzner J., and Bamler R. (2002) "Burst-mode and ScanSAR interferometry," in IEEE Transactions on Geoscience and Remote Sensing, vol. 40(9), pp. 1917–1934.

[2] De Zan F., and Monti Guarnieri A. (2006). "TOPSAR: Terrain Observation by Progressive Scans", IEEE Transactions on Geoscience and Remote Sensing, vol. 44(9), pp. 2352–2360.

[3] Scheiber R. and Moreira A. (2000). "Coregistration of interferometric SAR images using spectral diversity", IEEE Transactions on Geoscience and Remote Sensing, vol. 38 (5), pp. 2179–2191.

[4] Prats-Iraola P., Scheiber R., Marotti L., Wollstadt S., and Reigber A. (2012). "TOPS Interferometry With TerraSAR-X", IEEE Transactions on Geoscience and Remote Sensing, vol. 50(8), pp. 3179–3188.

[5] Prats-Iraola P., Yague-Martinez N., Wollstadt S., Kraus T., and Scheiber R. (2016). "Demonstration of the Applicability of 2-Look Burst Modes in Non-Stationary Scenarios with TerraSAR-X," Proceedings of EUSAR 2016: 11th European Conference on Synthetic Aperture Radar, Hamburg, Germany, pp. 1–6.

[6] Torres R., Snoeij P., Geudtner D., Bibby D., Davidson M., Attema E., Potin P., Rommen B., Floury N., Brown M., Navas Traver I., Deghaye P., Duesmann B., Rosich B., Miranda N., Bruno C., L'Abbate M., Croci R., Pietropaolo A., Huchler M., and Rostan F. (2012). "GMES Sentinel-1 mission", Remote Sensing of Environment, vol. 120, pp. 9–24.

[7] Yagüe-Martínez N., Prats-Iraola P., Rodríguez González F., Brcic R., Shau R., Geudtner D., Eineder M., and Bamler R. (2016). "Interferometric Processing of Sentinel-1 TOPS Data", IEEE Transactions on Geoscience and Remote Sensing, vol. 54(4), pp. 2220–2234.

[8] Scheiber R., Jäger M., Prats-Iraola P., De Zan F., and Geudtner D. (2015). "Speckle Tracking and Interferometric Processing of TerraSAR-X TOPS Data for Mapping Nonstationary Scenarios," in IEEE Journal of Selected Topics in Applied Earth Observations and Remote Sensing, vol. 8(4), pp. 1709–1720.

[9] Prats-Iraola P. et al. (2017). "Interferometric investigations with the Sentinel-1 constellation," 2017 IEEE International Geoscience and Remote Sensing Symposium (IGARSS), Fort Worth, TX, USA, pp. 5537–5540.

[10] Solgaard A., Kusk A., Merryman Boncori J. P., Dall J., Mankoff K., Ahlstrøm A., Andersen S., Citterio M., Karlsson N., Kjeldsen K., Korsgaard N., Hillerup Larsen S., Fausto R. (2021). "Greenland ice velocity maps from the PROMICE project," Earth System Science Data. vol. 13, pp. 3491–3512.

[11] Okada Y. (1985). "Surface Deformation due to Shear and Tensile Faults in a Half-Space," Bulletin of the Seismological Society of America, vol. 75, pp. 1135–1154.

[12] Ronneberger O., Fischer P., and Brox T. (2015). "U-Net: Convolutional networks for biomedical image segmentation," Proc. Int. Conf. Med. Image Comput. Comput.-Assist. Intervent., pp. 234–241.

[13] Solgaard A., and Kusk A. (2021). "Winter Ice Velocity Mosaics for the Greenland Ice Sheet from Sentinel-1 Edition 1," GEUS Dataverse, V3.